Available online at www.sciencedirect.com

SCIENCE DIRECT®

Earth and Planetary Science Letters 227 (2004) 73–85

EPSL

www.elsevier.com/locate/epsl

Deep global cycling of carbon constrained by the solidus of anhydrous, carbonated eclogite under upper mantle conditions

Rajdeep Dasgupta*, Marc M. Hirschmann, Anthony C. Withers

Department of Geology and Geophysics, University of Minnesota, 310 Pillsbury Drive SE, Minneapolis, MN 55455, USA

Received 4 March 2004; received in revised form 16 July 2004; accepted 6 August 2004
Available online 15 September 2004
Editor: K. Farley

Abstract

We present partial melting experiments that constrain the near solidus phase relations of carbonated eclogite from 2 to 8.5 GPa. The starting material was prepared by adding 5 wt.% CO_2 in the form of a mixture of Fe–Mg–Ca–Na–K carbonates to an eclogite from Salt Lake crater, Oahu, Hawaii and is a reasonable approximation of carbonated oceanic crust from which siliceous hydrous fluids have been extracted during subduction. Melt-present versus melt-absent conditions are distinguished based on textural criteria. Garnet and clinopyroxene appear in all the experiments. Between 2 and 3 GPa, the subsolidus assemblage also includes ilmenite±calcio-dolomite$_{ss}$±CO_2, whereas above the solidus (1050–1075 °C at 3 GPa) calcio-dolomitic liquid appears. From 3 to 4.5 GPa, dolomite$_{ss}$ is stable at the solidus and the near-solidus melt becomes increasingly dolomitic. The appearance of dolomite above 3 GPa is accompanied by a negative Clapeyron slope of the solidus, with a minimum located between 995 and 1025 °C at ca. 4 GPa. Above 4 GPa, the solidus rises with increasing pressure to 1245±35 °C at 8.5 GPa and magnesite becomes the subsolidus carbonate. Dolomitic melt coexists with magnesite+garnet+cpx+rutile along the solidus from 5 to 8.5 GPa.

Comparison of our results to other recent experimental studies [T. Hammouda, High-pressure melting of carbonated eclogite and experimental constraints on carbon recycling and storage in the mantle, Earth Planet. Sci. Lett. 214 (2003) 357–368; G.M. Yaxley, G.P. Brey, Phase relations of carbonate-bearing eclogite assemblages from 2.5 to 5.5 GPa: implications for petrogenesis of carbonatites, Contrib. Mineral. Petrol. 146 (2004) 606–619] shows that carbonate minerals are preserved in anhydrous or slightly hydrous carbonated eclogite to temperatures >1100 and >1200 °C at 5 and 9 GPa, respectively. Thus, deep subduction of carbonate is expected along any plausible subduction geotherm. If extrapolated to higher pressures, the carbonated eclogite solidus is likely to intersect the oceanic geotherm at a depth close to 400 km. Carbonated eclogite bodies entering the convecting upper mantle will thus release carbonate melt near the top of the mantle transition zone and may account for anomalously slow seismic velocities at depths of 280–400 km. Upon release, this small volume, highly reactive melt could be an effective agent of deep mantle metasomatism. Comparison of the carbonated eclogite solidus with that of peridotite-CO_2 shows a shallower solidus–geotherm intersection for the latter. This implies that carbonated peridotite is a more likely proximal source of magmatic carbon in oceanic provinces. However, carbonated eclogite is a potential source of continental carbonatites, as its solidus crosses the continental shield geotherm at

* Corresponding author. Tel.: +1 612 625 0366; fax: +1 612 625 3819.
E-mail address: dasg0007@umn.edu (R. Dasgupta).

0012-821X/$ - see front matter
doi:10.1016/j.epsl.2004.08.004

ca. 4 GPa. Transfer of eclogite-derived carbonate melt to peridotite may account for the geochemical characteristics of some oceanic island basalts (OIBs) and their association with high CaO and CO_2.

Keywords: carbon cycle; experimental petrology; partial melting; eclogite; ocean island basalts

1. Introduction

Cycling of carbon into and out of the mantle plays a key role in the global carbon cycle and influences the CO_2 budget of the Earth's atmosphere. Subduction introduces carbon into the mantle, while volcanic outgassing releases it to the surface. Calcium carbonate sequestered in oceanic crust by hydrothermal alteration accounts for a flux of $2.3–3.7\times10^{12}$ mol carbon/year into the mantle [3,4]. A significant portion of this carbonate resides in the top 300 m of altered basalts, where the average CO_2 content is ~3 wt.% [3] and most of this is believed to survive subduction-related dehydration or silicate melting [5–7]. Consequently, carbonated anhydrous eclogite may deliver significant carbon to the deeper mantle. Melting-induced release of carbonates from such eclogite thus affects the distribution of carbon in the deep Earth and so the location of the carbonated eclogite solidus at upper mantle conditions is a key factor in the deep carbon cycle. Release of carbonatite melts along subduction geotherms may extract carbon from subducting crust, whereas preservation of carbonate minerals would allow transport of carbon to the transition zone or to the lower mantle. Return of subducted carbonated eclogite to the upper mantle along the convecting mantle (ridge) adiabat may produce carbonatite melts in the deeper parts of the upper mantle, because the solidus of carbonated eclogite is probably exceeded to significant depth. Comparison of the solidus of carbonated eclogite to that of carbonated peridotite and to the oceanic-ridge geotherm should also constrain potential hosts for carbonate in the convecting upper mantle and identify potential sources of magmatic CO_2.

Recent experimental studies on partial melting of carbonated eclogite [1,2] yield notably different solidus locations and near-solidus phase relations. Here, we present new experimental determinations of the solidus and near solidus phase relations of carbonated eclogite from 2 to 8.5 GPa, compare these to other recent results, and relate them to the problem of global carbon cycling.

2. Experimental methods

Eclogite xenolith (66039B) from Salt Lake Crater, Hawaii was used as the silicate fraction for our experiments (Table 1). The rock powder was dried overnight at 1000 °C in a CO/CO_2 gas mixing furnace at log fO_2=QFM-1 and was then reground to ≤5 μm particles before the carbonate mixture was added. Relative to typical oceanic crust (Table 1), this eclogite is deficient in SiO_2, Al_2O_3, and Na_2O and more refractory (Mg#=100×molar Mg/(Mg+Fe_T)=64.13) (Table 1), as may be appropriate for subducted oceanic crust from which small degree of partial melts or siliceous hydrous fluids have been extracted [5,9]. To foster detection of melt, the CO_2 concentration in the material used in this study (5 wt.%) is somewhat higher than that in altered oceanic crust (2–3% by weight in the top 0.3 km [3,10] and ~0.3–0.5% by weight in the bulk crust ([3], Petdb database: http://petdb.ldeo.columbia.edu/petdb; Table 1). Ocean floor alteration adds veins of calcite to basaltic crust, but the Ca comes primarily from the silicate minerals in the basalt [3,10,11] and thus the abundance of Ca is not enhanced relative to other cations. In addition, subduction-induced dehydration likely elevates the Mg/Ca ratio of the bulk crust, as Ca is dissolved more efficiently than Mg [9]. For constructing carbonated experimental starting materials, introduction of CO_2 by addition of calcite enhances the Ca concentration. For this reason, we constructed the bulk starting composition by adding a mixture of synthetic (reagent grade Na_2CO_3, K_2CO_3, and $CaCO_3$) and natural (magnesite and siderite from University of Minnesota's mineral collection) carbonates such that Mg#, Ca# (=100× molar Ca/(Ca+Mg+Fe_T)), Na# (=100×molar Na/(Ca+Na+K)), and molar Na/(Na+K) were unaffected

Table 1
Composition of the starting material[a]

	66039B[b]	cpx[c]	gt	$MORB_8$[d]	Simple crust[e]	SLEC1	OTBC[f]	EC1[g]	alt-MORB[h]
SiO_2	46.34	50.27	40.66	50.26	50.64	41.21	47.23	30.11	49.16±1.55
TiO_2	2.43	1.25	0.29	1.43	1.11	2.16	–	–	1.43±0.61
Al_2O_3	12.25	7.97	23.15	15.43	15.50	10.89	15.35	11.74	15.54±1.49
Cr_2O_3	0.10	0.02	0.07	–	–	0.09	–	–	0.42+1.19/−0.42
FeO_T[i]	12.27	8.57	16.20	10.34	10.29	12.83	8.93	10.05	9.20±2.43
MnO	0.14	0.10	0.32	0.16	0.16	0.12	–	–	0.17±0.07
MgO	12.30	12.78	14.74	8.08	8.24	12.87	6.24	12.44	7.35±1.44
CaO	12.52	16.51	4.75	11.58	11.17	13.09	14.77	19.41	11.81±1.61
Na_2O	1.56	2.52	0.05	2.62	2.77	1.63	2.91	0.87	2.43±0.44
K_2O	0.11	n.a.	0.01	0.10	0.12	0.11	0.02	–	0.29+0.42/−0.29
CO_2						5.00	4.43	15.38	0.51+0.72/−0.51
H_2O						–	0.12	–	2.53+2.78/−2.53
P_2O_5						–	–	–	0.16±0.12
Total	100.00	99.99	100.22	100.00	100.00	100.00	99.88	100.00	
Mg#[j]	64.13	72.66	61.86	58.21	58.8	64.13	55.47	68.81	59.09±10.41
CaO/MgO[k]	0.73	0.93	0.23	1.03	0.97	0.73	1.7	1.12	1.20±0.29
Na_2O/CO_2[l]						0.23	0.47	0.04	11.59+14.02/−11.59

[a] SLEC1 is the starting material composition used in this study.
[b] 66039B gives the composition of the silicate portion of the starting material. Approximately 2 mg of the rock powder was fused in a graphite crucible in a one-atmosphere furnace for 10 min at 1300 °C. The composition of the starting silicate rock powder was determined by electron microprobe (EMP) analysis of this glass.
[c] cpx and gt gives the compositions of clinopyroxene and garnet in 66039B.
[d] Fresh, average MORB [8].
[e] Typical, average oceanic crust [8].
[f] Hammouda [1].
[g] Yaxley and Brey [2].
[h] Composition of the altered mid-ocean ridge basalts selected from Petdb database (http://petdb.ldeo.columbia.edu/petdb). Selected alteration types varied from mild to complete.
[i] Total Fe as Fe^{2+}.
[j] Molar $Mg/(Mg+Fe_T)\times 100$.
[k] Molar CaO/MgO.
[l] Molar Na_2O/CO_2.

by CO_2 addition. This approach minimizes the effect of overabundances of carbonate/CO_2 on the cationic proportions of the bulk starting composition and thus on the solidus temperature of anhydrous, carbonated eclogite. In a forthcoming contribution (Dasgupta et al., in preparation), we examine in greater detail the influence of the quantity and composition of added carbonate on eclogite solidus location.

Experiments were performed in piston cylinder (PC) (2–3.3 GPa) and multi-anvil (MA) (3.3–8.5 GPa) devices and run conditions are given in Table 2. A homogeneous mixture of carbonated eclogite powder (SLEC1; Table 1) was sealed in Pt capsules with graphite inner liners. End-loaded PC experiments were performed with a 1/2″ assembly ([8] and references therein). MA experiments were conducted in a 1000-ton Walker-type device. For MA experiments, WC anvils with 12 mm truncations, cast MgO–Al_2O_3–SiO_2–Cr_2O_3 octahedra with 18 mm edge lengths and integrated gasket fins, and straight-walled graphite heaters were used. The pressure calibration for this assembly was established against multiple high-temperature fixed points (Fig. 1). Temperature was controlled with a $W_3Re_{97}/W_{25}Re_{75}$ thermocouple next to the capsule and oriented axially with respect to the heater. *P–T* uncertainties are believed to be ±0.1 GPa, ±12 °C for PC ([8] and references therein) and ±0.3 GPa, ±10 °C for MA runs. To verify the consistency of the two apparatus, we bracketed the solidus temperature at 3.3 GPa in both MA and PC. Piston cylinder run times ranged from 6 to 96 h, except for experiment A435, which lasted 164 h in

Table 2
Summary of the run conditions and phase assemblages

Run	P (GPa)	T (°C)	t (h)	Phase assemblage[a]
A386	2.0	950	47	Gt+Cpx+Ilm+(Cc-Dol_{ss})[b]+ CO_2 vapor[c]
A385	2.0	975	26	Gt+Cpx+Ilm+(L_c)?+ CO_2 vapor
A377	2.5	1000	24	Gt+Cpx+Ilm+(Cc-Dol_{ss})+ CO_2 vapor
A384	2.5	1025	48	Gt+Cpx+Ilm+(L_c)?+ CO_2 vapor
A383	2.5	1050	50	Gt+Cpx+Ilm+(L_c)?+ CO_2 vapor
A378	2.5	1075	24	Gt+Cpx+Ilm+CO_2 vapor
A435	3.0	1010	164	Gt+Cpx+Ilm+Cc-Dol_{ss}
A372	3.0	1050	48	Gt+Cpx+Ilm+Cc-Dol_{ss}
A382	3.0	1075	96	Gt+Cpx+Ilm+L_c
A388	3.0	1080	22	Gt+Cpx+Ilm+L_c
A380	3.0	1100	24	Gt+Cpx+Ilm+L_c
A373	3.0	1125	25	Gt+Cpx+Ilm+L_c
A375	3.0	1150	6	Gt+Cpx+Ilm+L_c
A381	3.0	1175	24	Gt+Cpx+Ilm+L_c
A392	3.3	1025	21	Gt+Cpx+Ilm+Dol_{ss}+ *Mst*+*Sid*[d]
M92	3.3	1025	12	Gt+Cpx+Ilm+Dol_{ss}
M90	3.3	1060	12	Gt+Cpx+Ilm+Dol_{ss}+L_c
M85	3.3	1083	12	Gt+Cpx+Ilm+L_c
A391	3.38	1050	21	Gt+Cpx+Ilm+Dol_{ss}+ *Mst*+*Sid*+L_c
M95	4.1	995	12	Gt+Cpx+Ilm+Dol_{ss}+ *Sid*+*Mst*
M93	4.1	1025	12	Gt+Cpx+Ilm+Mst+*Sid*+(L_c)
M91	4.1	1075	12	Gt+Cpx+Mst+(Rut)+L_c
M86	4.1	1125	12	Gt+Cpx+(Rut)+(Mst)+L_c
M113	4.6	1010	24	Gt+Cpx+Ilm+Dol_{ss}+Mst
M96	5.1	1010	12	Gt+Cpx+Mst+(Rut)+*Sid*
M102	5.1	1050	12	Gt+Cpx+Rut+Mst+L_c
M110	5.6	1040	24	Gt+Cpx+Rut+Mst
M105	6.1	1080	12	Gt+Cpx+Rut+Mst+L_c
M104	7.0	1100	12	Gt+Cpx+Mst+(Rut)
M106	7.0	1130	12	Gt+Cpx+Rut+Mst+L_c
M130	8.5	1175	12	Gt+Cpx+Mst+(Rut)
M129	8.5	1210	12	Gt+Cpx+Mst+(Rut)
M131	8.5	1280	12	Gt+Cpx+(Rut)+L_c

Multi-anvil runs are prefixed with 'M'.

[a] Gt—garnet, Cpx—clinopyroxene, Mst—magnesite (Mg-rich $carbonate_{ss}$), Sid—siderite (Fe-rich $carbonate_{ss}$), Rut—rutile, Ilm—ilmenite, Cc-Dol_{ss}—Fe-bearing calcito-dolomitic solid solution, Dol_{ss}—dolomite–ankerite solid solution, L_c—carbonate melt.

[b] Phases within parentheses occupy less than 2 vol.% of the entire charge.

[c] CO_2 vapor is inferred to be present during the experiments from the presence of only trace amount of carbonate minerals or melts.

[d] Phases in italics are inferred to be unreacted metastable starting material present in trace amount.

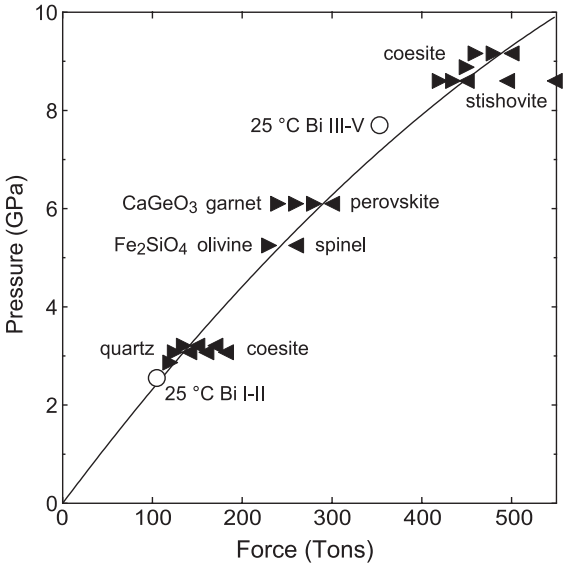

Fig. 1. Pressure calibration for the 12 mm truncated edge length (TEL) octahedral assembly in the Minnesota multi-anvil laboratory. The force–pressure relationship was calibrated against 25 °C fixed points of the Bi I–II and Bi III–V transitions [12] and high-temperature fixed points for quartz–coesite (1000 and 1200 °C) [13], Fe_2SiO_4 olivine–spinel (1000 °C) [14], $CaGeO_3$ garnet–perovskite (1000 °C) [15], and coesite–stishovite (1000 and 1350 °C) [16]. Bi transition points are averages from five experiments. The linear fit to the brackets is described by P (GPa)=0.024×Force (metric tons)−1.149×10^{-5}×Force (metric tons)^2.

order to enhance equilibration under subsolidus conditions. Multi-anvil runs were ≤24 h. Short run times were preferred to minimize the influx of hydrogen from the pressure assembly into the capsule [17]. The redox states during the experiments were not strictly controlled, but the reaction of graphite inner crucible with oxygen probably yielded an oxygen fugacity close to CCO ($2CO+O_2=2CO_2$) buffer at pressures up to ca. 4 GPa. At higher pressures, equilibria similar to $CaMg(CO_3)_2+2SiO_2=CaMgSi_2O_6+2C+O_2$ possibly controlled the fO_2 [18]. Run products were polished using polycrystalline-diamond paste. Owing to the soft and water-soluble character of quenched carbonate melt, water was avoided during polishing.

Run products were analyzed using a JEOL JXA8900R electron microprobe at the University of Minnesota with an accelerating voltage of 15 kV, 20 s peak counting times (10 s for carbonates) and a ZAF matrix correction routine. For silicates and oxide minerals, a focused 20 nA beam was used, but for

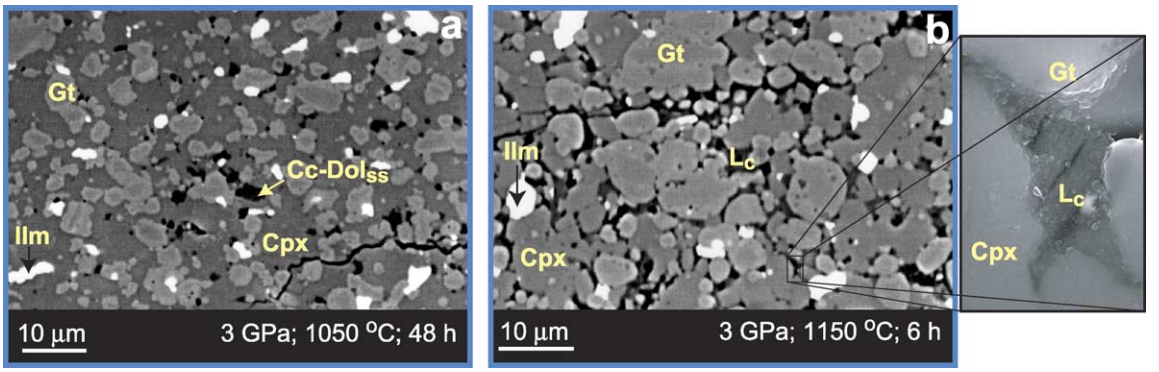

Fig. 2. Back-scattered electron images of the typical run products showing distinctions between melt-present and melt-absent conditions. Carbonate minerals or melts appear dark/dark gray. In a subsolidus run (a) discrete grains of carbonate minerals appear. Above the solidus (b), quenched carbonate melts are interstitial to the silicate grains and maintain a well-connected geometry. In addition, silicate grains in presence of melt (b) are larger, with faceted grain boundaries, and more homogeneous with respect to melt-absent runs. A high-resolution secondary electron image (inset to b) shows the texture of the quenched melt.

carbonate minerals and quenched melts we employed a defocused beam ranging from 1 to 3 μm diameter and a current of 1–3 nA, depending on the grain size or the dimension of the interstitial quenched melt pool. Natural clinopyroxene, garnet, hornblende, ilmenite, dolomite, and siderite were used as analytical standards. Textural interpretations of near-solidus melt were confirmed using a high-resolution SEM (JEOL JSM-6500F FEG-SEM) (see inset to Fig. 2b).

3. Experimental results

3.1. Texture

We detect the onset of partial melting in our experiments using textural criteria. Below the solidus, carbonate occurs only as discrete mineral grains (Fig. 2a), but above the solidus, quenched carbonate melt is observed in triple grain junctions and along grain edges between silicate phases (Fig. 2b). In some melt-present experiments, silicate grains show rounded forms (Fig. 2b), faceted grain boundaries, and melt concentrates towards the top of the capsule (not shown). Few faceted grains are apparent below the solidus and mineral zoning is more pronounced (Fig. 2a). Finally, grain growth is faster when melt is inferred to be present; i.e., the mineral grains in the experiment illustrated in Fig. 2b are much larger than the one shown Fig. 2a, even though the run duration in Fig. 2a was eight times longer.

3.2. Solidus location and near solidus phase assemblages

A summary of the run conditions with corresponding phase assemblages for SLEC1 is given in Table 2. The location of the solidus is plotted in Fig. 3 along

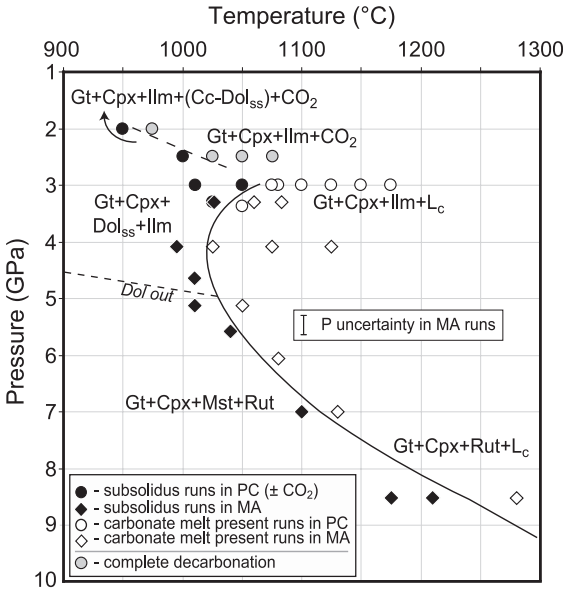

Fig. 3. Experimental constraints on the solidus of carbonated eclogite (SLEC1). Phase abbreviations as in Table 2. Phases within parentheses are present in trace amount. Pressure–temperature uncertainties for piston cylinder (PC) runs (±0.1 GPa, ±12 °C) and temperature uncertainty for multi-anvil (MA) runs (±10 °C) are within size of the symbols.

Table 3
Phase compositions (in wt.%) from the partial melting experiments of SLEC1[a]

Run	Phase[b]	w.f.[c]	n[d]	SiO_2	TiO_2	Al_2O_3	Cr_2O_3	FeO_T	MnO	MgO	CaO	Na_2O	K_2O	Na_2O calc.[e]	CO_2[f]	Sum[g]
A372	cpx	0.50	11	52.36(33)	0.54(9)	4.79(66)	0.02(2)	7.98(42)	0.11(3)	14.93(37)	16.70(58)	2.08(16)	0.02(1)		–	99.53(66)
	gt	0.38	5	39.44(14)	0.72(16)	21.86(28)	0.05(3)	18.35(26)	0.35(3)	13.35(29)	5.89(25)	0.09(2)	0.03(1)		–	100.13(21)
	ilm	0.03	3	0.20(8)	50.67(17)	0.50(3)	0.05(1)	40.45(19)	0.18(4)	7.28(22)	0.60(7)	0.02(3)	0.04(3)		–	100.00(31)
	cc-dol_{ss}	0.08	3	0.07(5)	0.04(3)	0.09(7)	n.a.[h]	9.01(110)	0.21(5)	16.67(62)	27.97(76)	0.03(1)	0.01(2)		45.90	100.00
A382	cpx	0.47	7	53.23(43)	0.54(5)	4.08(31)	0.03(2)	7.92(23)	0.09(2)	15.64(38)	17.22(42)	1.74(12)	0.00		–	100.49(84)
	gt	0.40	14	39.73(19)	0.59(16)	22.22(25)	0.04(3)	17.38(34)	0.33(3)	13.92(42)	5.57(43)	0.33(31)	0.02(1)		–	100.13(44)
	ilm	0.04	1	0.26	49.95	0.75	0.06	41.29	0.15	6.70	0.68	0.13	0.04		–	100.00
	L_c	0.09	4	1.88(29)	0.02(3)	0.76(36)	n.a.	10.02(108)	0.22(7)	12.20(53)	31.16(37)	0.89(52)	0.07(5)	7.54	42.78	100.00
A380	cpx	0.47	5	53.68(23)	0.58(6)	4.31(21)	0.01(2)	8.16(14)	0.01(3)	14.73(33)	17.00(44)	1.71(6)	0.00(1)		–	100.19(65)
	gt	0.40	3	39.30(17)	0.64(13)	21.90(31)	0.09(1)	17.05(29)	0.40(4)	13.83(31)	5.86(36)	0.13(4)	0.05(2)		–	99.26(67)
	ilm	0.04	2	0.34	49.70	0.93	0.00	40.57	0.00	6.25	0.93	0.37	0.00		–	99.10
	L_c	0.09	4	2.21(41)	0.01(2)	0.79(31)	0.02(1)	8.81(97)	0.83(4)	10.07(31)	31.28(36)	1.81(32)	0.18(2)	8.12	43.99	100.00
M90	cpx		7	53.18(42)	0.54(6)	4.28(40)	0.03(3)	7.88(43)	0.10(2)	15.62(29)	16.44(70)	1.83(18)	0.01(1)		–	99.91(44)
	gt		3	41.20(66)	0.69(1)	20.53(25)	0.02(2)	16.45(63)	0.30(5)	13.49(44)	7.01(15)	0.30(8)	0.03(1)		–	99.99(2)
	ilm		2	0.62	50.16	0.72	0.02	39.82	0.19	7.51	0.71	0.22	0.03		–	100.00
M85	cpx		10	53.49(25)	0.54(5)	4.12(36)	0.03(2)	7.66(54)	0.09(2)	15.53(44)	16.77(90)	1.83(16)	0.01(1)		–	100.07(30)
	gt		10	40.34(52)	0.65(9)	22.25(24)	0.01(1)	16.60(37)	0.30(4)	13.96(27)	5.92(28)	0.18(14)	0.03(1)		–	100.24(56)
	ilm		2	0.26	50.12	0.58	0.00	40.42	0.21	7.49	0.67	0.21	0.03		–	100.00
A391	cpx		2	52.98	0.60	5.44	0.05	8.01	0.09	14.09	16.48	2.48	0.01		–	100.24
	dol_{ss}		1	0.54	0.09	0.06	n.a.	7.42	0.94	18.90	27.52	0.00	0.00		44.53	100.01
M93	cpx		1	54.00	0.48	5.05	0.00	6.74	0.05	13.65	17.10	2.89	0.03		–	100.00
	ilm		2	0.38	50.45	0.38	0.00	42.72	0.21	4.96	0.70	0.19	0.02		–	100.00
M91	cpx		6	52.94(42)	0.61(14)	4.59(36)	0.03(2)	8.57(10)	0.06(2)	13.25(25)	17.18(32)	2.75(14)	0.02(1)		–	100.00(43)
	gt		6	40.00(69)	1.38(94)	20.95(30)	0.01(1)	18.03(26)	0.28(3)	11.78(29)	6.87(31)	0.21(5)	0.03(1)		–	99.54(69)
	L_c		2	2.13	0.09	0.68	n.a.	8.95	0.12	17.35	24.15	0.27	0.02		46.24	100.00
M86	cpx	0.46	6	53.74(27)	0.58(5)	4.56(20)	0.03(3)	8.43(20)	0.09(1)	14.32(27)	15.97(32)	2.45(7)	0.02(2)		–	100.17(45)
	gt	0.41	12	39.61(40)	1.08(20)	21.33(25)	0.02(2)	18.33(46)	0.28(3)	12.22(55)	6.42(51)	0.18(5)	0.03(1)		–	99.51(54)
	rut[i]	0.01														
	mst[j]	0.00	1	0.04	0.03	0.04	0.03	13.65	0.01	29.73	6.28	0.09	0.09		50.02	100.00
	L_c	0.12	2	3.65	0.15	0.75	0.00	9.10	0.24	17.02	24.03	0.19	0.04	3.69	44.84	100.00
M102	cpx		10	53.94(43)	0.47(5)	4.21(23)	0.04(2)	7.92(22)	0.09(3)	14.08(29)	16.76(46)	2.45(14)	0.02(1)		–	99.97(42)
	gt		7	39.86(31)	0.94(7)	21.32(30)	0.02(1)	19.39(24)	0.31(3)	12.00(43)	7.21(44)	0.18(4)	0.02(1)		–	101.25(37)

(continued on next page)

Table 3 (*continued*)

Run	Phase[b]	w.f.[c]	n[d]	SiO_2	TiO_2	Al_2O_3	Cr_2O_3	FeO_T	MnO	MgO	CaO	Na_2O	K_2O	Na_2O calc.[e]	CO_2[f]	Sum[g]
M110	cpx		2	52.33	0.61	5.48	0.00	7.24	0.06	12.60	18.26	2.69	0.02		–	99.29
	gt		1	37.84	0.93	21.39	0.02	19.98	0.37	10.44	8.84	0.20	0.05		–	100.05
M105	cpx		3	53.63(67)	0.37(1)	4.63(24)	0.04(5)	7.19(19)	0.08(0)	13.31(11)	18.15(50)	2.83(8)	0.05(1)		–	100.29(26)
	gt		2	39.03	1.01	20.39	0.01	19.95	0.33	10.32	9.01	0.25	0.02		–	100.32
M104	cpx	0.46	5	52.83(30)	0.50(14)	4.96(17)	0.02(2)	7.39(36)	0.12(3)	12.47(54)	17.77(46)	3.26(10)	0.04(2)		–	99.36(87)
	gt	0.43	11	39.52(62)	1.41(17)	19.98(28)	0.01(2)	18.63(37)	0.32(3)	9.50(45)	10.48(46)	0.26(5)	0.03(2)		–	100.15(55)
	rut	0.01														
	mst	0.10	1	0.06	0.02	0.02	n.a.	16.27	0.06	32.75	2.82	0.00	0.04		47.94	100.00
M130	cpx	0.45	11	53.55(55)	0.50(13)	4.78(25)	0.01(2)	7.33(12)	0.07(3)	12.42(47)	17.66(39)	3.54(26)	0.05(2)		–	99.91(28)
	gt	0.44	6	38.77(55)	1.75(36)	19.49(14)	0.02(2)	18.81(21)	0.31(3)	10.08(33)	9.78(23)	0.49(48)	0.02(1)		–	99.52(51)
	rut	0.01	6													
	mst	0.09	4	0.06(2)	0.02(1)	0.04(2)	0.01(2)	15.66(11)	0.13(3)	32.52(35)	3.27(20)	0.00(1)	0.02(2)		48.27	100.00
M129	cpx	0.44	8	52.66(89)	0.36(5)	4.57(23)	0.01(1)	6.69(16)	0.08(3)	13.44(24)	17.96(30)	3.25(11)	0.06(1)		–	99.08(95)
	gt	0.45	5	39.87(50)	1.68(29)	19.57(10)	0.02(3)	19.05(29)	0.32(3)	10.17(42)	10.25(19)	0.32(5)	0.03(1)		–	101.28(55)
	rut	0.01														
	mst	0.09	2	0.02	0.02	0.11	n.a.	15.14	0.00	34.18	2.20	0.00	0.06		48.00	100.00
M131	cpx	0.40	17	53.79(73)	0.44(4)	4.38(18)	0.02(2)	7.16(24)	0.07(3)	13.59(29)	17.30(35)	2.78(14)	0.04(1)		–	99.57(72)
	gt	0.49	6	40.19(77)	1.65(18)	19.39(16)	0.03(2)	17.34(51)	0.27(2)	13.11(37)	8.17(41)	0.50(35)	0.02(1)		–	100.65(35)
	rut	0.01														
	L_c	0.10	2	1.15	0.29	0.16	n.a.	13.74	0.08	14.03	26.06	0.22	0.02	2.76	44.26	100.00

[a] Numbers in parentheses are one standard deviation in terms of last digit(s). Thus, 52.36(33) should be read as 52.36±0.33. Standard deviations are reported only when there are at least three points to average.

[b] Phase abbreviations as in Table 2.

[c] Weight fractions determined by mass balance calculations and could not be determined for all the experiments as one of the phases could not be analyzed due to fine grain size.

[d] Number of analyses considered to give equilibrium compositions averaged.

[e] Concentration of Na_2O calculated by mass balance to achieve zero residual for the same [19].

[f] CO_2 is calculated by difference of 100 and the measured analytical total.

[g] For all the phases apart from carbonate minerals or melts, analytical totals are given (except where the totals are reported in italics; in these, analytical totals were low—ilm: 95–97 wt.%, gt: 96–98 wt.%—owing to difficulty in analyzing very small grains).

[h] Element not analyzed.

[i] WDS quantitative analyses cannot be performed due to fine grain size (<2 μm). However, EDS spectra showed no other element peaks other than that of Ti and thus end-member TiO_2 composition is used for mass balance calculation.

[j] Calculated fraction for $magnesite_{ss}$ in run M86 is zero, however, $magnesite_{ss}$ is present in trace quantity.

with the near-solidus phase assemblages. Garnet and clinopyroxene are present in all experiments. Ilmenite is stable along the solidus to just below 5 GPa, where it is replaced by rutile.

A CO_2-rich vapor phase is inferred as the major host of carbon for all the runs at 2 and 2.5 GPa, as only traces of carbonate phases (crystal or melt) are observed; no similar evidence of decarbonation is observed at ≥3 GPa. Calcio-dolomitic solid solution (Cc-Dol_{ss}; Ca/(Ca+Mg)>0.5) is present at 2 to 3 GPa between 950 and 1050 °C. A trace of calcio-dolomitic liquid seems to appear at 2 GPa and 975 °C and at 2.5 GPa and 1025 °C. However, we are not certain about the presence of carbonate liquid in these two runs as the very small grain size makes it difficult to resolve the texture and hence is not shown in Fig. 3. At 3 GPa, calcio-dolomitic melt (L_c) is observed at 1075 °C and the temperature range for coexistence of Cc-Dol_{ss} and carbonate melt is narrow; i.e., crystalline carbonate phase disappears 30 °C above the solidus (1050–1075 °C). From 3.3 to 4.5 GPa, dolomitic solid solution (Dol_{ss}; Ca/(Ca+Mg) ≤0.5) remains stable below the solidus, near solidus carbonate melt becomes dolomitic, and the solidus temperature diminishes owing to the shift of the calcite–magnesite binary minimum to more Mg-rich compositions with increasing pressure [20]. The slope of the solidus becomes positive above ~4 GPa, and at ≥4 GPa, magnesite appears at the solidus (Fig. 3). At ≥5 GPa, dolomite is absent and dolomitic melt coexists with magnesite along the solidus from 5 to 8.5 GPa. Carbonatitic melt remains stable at least 100 °C above the solidus (1025–1125 °C) in presence of magnesite at 4.1 GPa (a depth of ca. 130 km) and ~100 °C above the solidus (1075–1175 °C) at 3 GPa (a depth of ca.100 km). Above 4 GPa, the solidus rises with increasing pressure: at 5.1 GPa the first melt appears at 1050 °C, at 7 GPa the solidus is located between 1100 and 1130 °C, and at 8.5 GPa it is between 1210 and 1280 °C.

3.3. Phase compositions

Phase compositions of the run products are given in Table 3. Owing to low run temperatures, experimental charges produced incompletely equilibrated textures. For example, unreacted cores of garnet and clinopyroxene persisted in experiment A435 even after 164 h at 3 GPa and 1010 °C. An approach to equilibrium, however, is verified by migration of the residual mineral rim compositions (Table 3) away from the starting compositions (Table 1), following the method of Pertermann and Hirschmann [21]. The data in Table 3 represent compositions of equilibrated mineral grains, rims, or melt pools determined from microprobe analyses that lack evidence of bias from beam overlap with neighboring phases or unreacted cores.

Quenched carbonate melt is calcio-dolomitic to dolomitic with Ca/(Ca+Mg) of 0.65–0.69 at 3 GPa, 0.50 at 4.1 GPa, and ~0.57 at 8.5 GPa, and always has higher Ca/Mg and lower Mg# than crystalline subsolidus carbonate at any given pressure (Table 3). As the subsolidus carbonate becomes magnesitic with increasing pressure, residual garnet becomes more calcic, increasing from ~6 to ~10 wt.% between 3 and 8.5 GPa. Garnet also becomes richer in TiO_2 with increasing pressure (Table 3). In clinopyroxenes, the Mg# varies between 72 and 78 and the principal shift is an increase in Na_2O with increasing pressure. A drop in Na_2O in clinopyroxene is noticed with increasing temperature across the solidus and/or with higher extent of melting at any given pressure, indicating partitioning of Na in near solidus carbonate liquid. However, Na concentrations in the reported melt analyses are low and we suspect partial loss of Na during polishing and/or migration of Na away from the electron beam during microprobe analyses. Reconstruction of the melt compositions to achieve zero residuals for sodium in the mass balance [19], yielded 2.76 (at 8.5 GPa) to 8.12% (at 3.0 GPa) Na_2O by weight (Table 3).

4. Discussion

4.1. Influence of bulk composition on the solidus of carbonated eclogite: comparison with other studies

The solidus established for carbonated eclogite SLEC1 is distinct from recent determinations by Hammouda [1] (composition "OTBC"—Table 1) and Yaxley and Brey [2] (composition "EC1"—Table 1) (Fig. 4). These differences are partly attributable to systematic bulk compositional effects, but may also partly reflect inter-laboratory biases. Key influences on

the solidus of carbonated lithologies include the Ca/Mg ratio of the carbonated portion of the whole rock, the bulk Na_2O/CO_2 ratio, and the presence of H_2O.

Because the minimum melting temperature in the binary $CaCO_3$ (Cc)–$MgCO_3$ (Mst) occurs at intermediate Ca/Mg ratios [20], rocks with calcite in the residue melt at higher temperature. Thus, the high solidus temperatures observed for EC1 [2] (Fig. 4) are likely owing to stabilization of calcite by the large amount of added $CaCO_3$ (35 wt.%). Similarly, the high solidus below 6.5 GPa for OTBC [1] (Fig. 4) is owing to high bulk Ca/Mg, which stabilizes refractory calcite in the near-solidus residue to high pressure. The sudden drop in solidus between 6 and 6.5 GPa noted for OTBC [1] and the analogous but less-dramatic drop for SLEC1 at ~4 GPa (Fig. 4) corresponds to stabilization of dolomite in the residue.

Another key effect is the Na_2O/CO_2 ratio of the starting material. A low molar Na_2O/CO_2 leads to low Na_2O in near-solidus carbonate liquids and thereby limits the fluxing effect of alkalis [2,22,23]. The low Na_2O/CO_2 (0.04) in EC1 [2] likely increases its solidus temperature relative to SLEC1 (0.23) and high Na_2O/CO_2 (0.47) may partially account for the low solidus temperatures of OTBC at high pressures (>6 GPa) [1]. However, the clinopyroxenes in these high-pressure experiments have 6.5–9.3 wt.% Na_2O [1], which limits the availability of Na_2O as a fluxing agent.

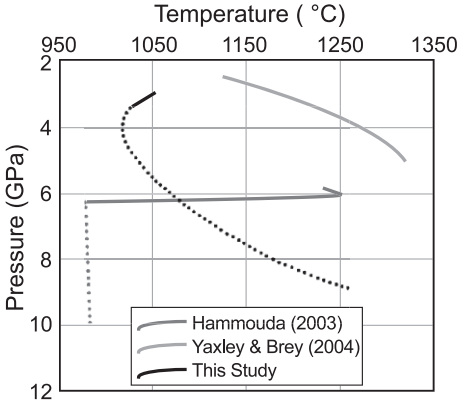

Fig. 4. Comparison of carbonated eclogite solidi from different studies ([1,2] and this study). Solid lines indicate stability of calcite or calcio-dolomitic solid solution at the solidus, whereas dotted line segments indicate stability of dolomite or magnesite solid solution. Minima in solidi from this study and that of Hammouda [1] correspond to the onset of dolomite stability.

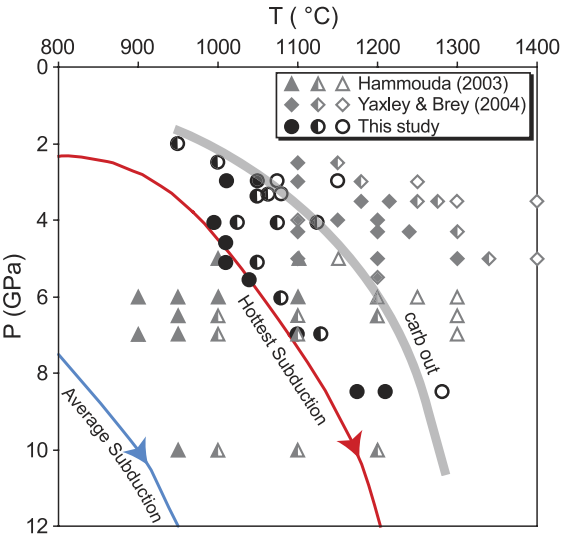

Fig. 5. *P–T* locations of different subduction geotherms [25,26] with respect to stability of crystalline carbonates in the residue of various carbonated eclogite partial melting experiments ([1,2]; this study). Filled symbols—carbon is present only as residual carbonate minerals; partially filled symbols—carbon is present both as minerals and as carbonatitic melt and/or vapor; open symbols—carbon is present only as carbonatitic melt or vapor. For the present study and that of Hammouda [1], the limit of stability of solid carbonate (indicated by shaded line marked "carb out") is ~100 °C above the hottest estimate of subduction geotherm [26]; for the study of Yaxley and Brey [2], carbonates remain to yet higher temperatures. Thus, melting will not eliminate carbonate from eclogite along any plausible subduction geotherm.

Minor amounts of H_2O may greatly lower the solidus of carbonated eclogite, and so the 1200-ppm H_2O in OTBC [1] may be the chief reason why the reported solidus is 100–250° lower than that observed for SLEC1 (Fig. 4). However, because of the exceptionally high solubility of H_2O in carbonate melts [24], small amounts of H_2O cannot induce significant carbonatite melt fractions far below the nominally anhydrous solidus. Thus, if the H_2O/CO_2 ratio is low, only a small portion of carbonate in eclogite will be removed by hydrous carbonated melting; most should remain until the nominally anhydrous solidus is approached. Indeed, Hammouda [1] noted carbonate minerals to 200 °C above his reported solidus (compare Figs. 4 and 5) from 6 to 10 GPa, temperatures similar to the solidus of SLEC1 (Figs. 3 and 4).

Because ocean floor alteration adds variable quantities and compositions of carbonate, leading to variations in Ca/Mg, Na_2O/CO_2 and H_2O/CO_2 of

affected basalts [3], there is no unique solidus that describes partial melting of carbonated eclogite. Although the quantitative effects of these variations are not yet fully established, we believe that the solidus established for SLEC1 is likely to be more closely applicable to subducted carbonated eclogite than EC1 or OTBC, owing to the large amount of added $CaCO_3$ in EC1 and the high Ca/Mg and added H_2O in OTBC.

In the following sections, we compare the solidus of SLEC1 with pressure–temperature conditions relevant for different domains of the mantle and discuss the consequences for the deep global carbon cycle.

4.2. Deep recycling of carbonates

Experiments and phase equilibria calculations suggest that oceanic crust is almost completely dehydrated in the first ~200 km of subduction [7,27,28], though minor amounts (<0.1–0.3 wt.%) of H_2O may be retained to greater depths in phengite [27] or in nominally anhydrous minerals [29]. Consequently, the nominally anhydrous solidus of carbonated eclogite controls whether carbonate will be expelled from subducting crust to the surrounding mantle. The solidus determined for SLEC1 remains hotter than the range of typical subduction geotherms, at least until the transition zone (>410 km), and appears not to intersect even the hottest subduction geotherms in the upper mantle (Fig. 6). This suggests that melting-induced release of carbonates from the subducting crust will not occur at least until the slab reaches the base of the upper mantle and thus subduction of carbonates into the lower mantle is likely.

The low-temperature solidus of OTBC [1] may apply to conditions under which carbonated eclogite dehydration is incomplete. However, water-enhanced melting will eliminate carbonate only for compositions with high H_2O/CO_2. Given that H_2O/CO_2 decreases during progressive metamorphism [6,7] and silicate melting of subducting slabs [5], this likely applies only to compositions with very low initial CO_2.

The chief consideration regarding delivery of CO_2 to the deep mantle by subducted carbonated eclogite is not whether the solidus is encountered

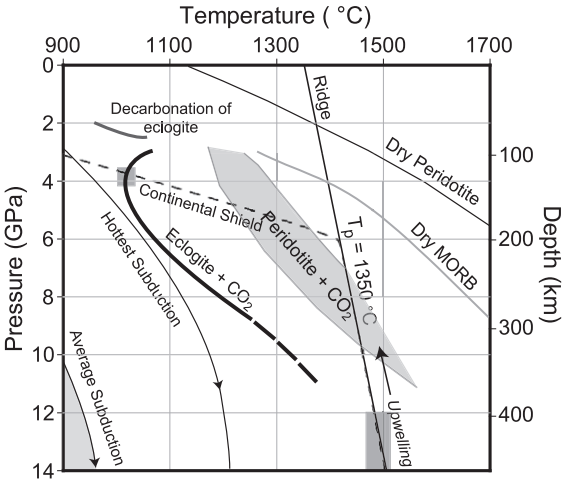

Fig. 6. Location of carbonated eclogite (SLEC1) solidus (Eclogite+CO_2) in relation to oceanic ridge geotherm (mantle potential temperature, T_p=1350 °C; [30]), calculated P–T conditions for subducting crust [25,26], and continental shield geotherm (40 mW/m^2) [31]. Also shown for reference are solidus of dry peridotite [22] and dry MORB [32]. Field of 'peridotite+CO_2' is bound by two different estimates of carbonated peridotite solidus [33,34] in the model CMAS–CO_2 system. Shaded region in the bottom left corner of the figure represents best estimate of subduction zone P–T conditions [25] along with the maximum estimate of expected temperature at depth ('Hottest Subduction', [26]). Gray-shaded boxes show likely conditions of generation of carbonate melt within eclogite in Earth's upper mantle for continental shield and convecting mantle settings.

along the subduction geotherm, but rather whether a significant portion of crystalline carbonate is preserved in the residue along that path. As illustrated in Fig. 5, all experimental results on partial melting of carbonated eclogite ([1,2]; this study) show that elimination of carbonate from the residue of eclogite requires temperatures ~100 °C hotter than any plausible subduction geotherm. Thus, even if modest amounts of carbonate are removed during subduction, some portion is delivered to the deeper mantle.

4.3. Return of carbonated eclogite to the upper mantle

Carbonated eclogite delivered to the transition zone or lower mantle may eventually be returned to the upper mantle by convection. Although pressure-dependent redox reactions may reduce the carbonate to diamond at great depths [35], this reaction would reverse on return to the upper mantle. If extrapolated to higher pressures, the solidus of SLEC1 intersects

the oceanic ridge-geotherm at ≥12–16 GPa (a depth of ca. 400–530 km) (Fig. 6). Thus, eclogite cannot host carbonate in the upper part of the oceanic upper mantle. Bodies of carbonated eclogite advected into the upper mantle would produce carbonatitic melt. Such melts may account for regions of anomalously slow seismic velocities observed at depths of 280–400 km [36–38].

4.4. Carbonatite liquids in the upper mantle

During advection in the upper mantle, the solidus of carbonated eclogite SLEC1 occurs 100–200 km deeper than that of carbonated peridotite [33,34] (Fig. 6). Small volume, highly mobile [39] carbonatitic melts released from eclogite at depths near 300–400 km could be an effective metasomatic agent [40,41] for surrounding peridotite. Observed signatures of recycled crust in many OIBs, such as high-μ ($^{238}U/^{204}Pb$), $^{87}Sr/^{86}Sr$, Ba, Th, LREE, Pb, and low $^{143}Nd/^{144}Nd$, Ti, Zr, Hf relative to MORB [42,43], may reflect metasomatic-implantation of eclogite-derived carbonate melt in shallower OIB source mantle. This may also explain the correlation between such recycling signatures and enrichments in CO_2 and/or CaO in many OIBs [40,44,45] and can also explain why erupted carbonatites commonly are associated with signatures of crustal recycling [46].

Continental shield geotherm intersects the carbonated eclogite solidus at ~130 km (Fig. 6). Thus, in portions of continental lithosphere consisting of former subducted slabs (e.g. [47]), carbonated eclogite could be a proximal source of carbonatites [48] and of CO_2-rich metasomatic fluid [41,49] derived from the continental lithosphere. Also, in contrast to the oceanic environment, carbonated peridotite melts deeper than carbonated eclogite along a continental geotherm (Fig. 6) so peridotite-derived carbonatitic melts may metasomatize eclogite in this environment.

5. Conclusions

The solidus of carbonated eclogite SLEC1 is hotter than plausible subduction geotherms but cooler than the geotherm of the oceanic mantle to depths near ~400 km. Thus, subduction is likely to introduce carbonated eclogite to significant mantle depths. On return to the convecting upper mantle, carbonated eclogite expels a carbonatitic melt. This melt is likely implanted into surrounding peridotite, owing to the much higher solidus of carbonated peridotite. In upwelling plumes, infiltration of eclogite-derived carbonatite melt into peridotite may explain the link between signatures of recycling and high-CaO and/or CO_2 in many OIBs.

Acknowledgements

We thank V.R. Murthy for the sample of Salt Lake crater xenolith. Greg Yaxley and Tahar Hammouda are acknowledged for their supportive reviews. R.D. thanks Jennifer Engstrom for help with the experiments in the initial stage of the investigation and Cyril Aubaud for numerous useful discussions and comments during preparation of the manuscript. R.D. also acknowledges support from the Dennis fellowship and V.R. Murthy and J. Noruk fellowship of the Department of Geology and Geophysics of the University of Minnesota. This work was supported by National Science Foundation grants OCE-9876255 and EAR-0310142 to Marc M. Hirschmann.

References

[1] T. Hammouda, High-pressure melting of carbonated eclogite and experimental constraints on carbon recycling and storage in the mantle, Earth Planet. Sci. Lett. 214 (2003) 357–368.
[2] G.M. Yaxley, G.P. Brey, Phase relations of carbonate-bearing eclogite assemblages from 2.5 to 5.5 GPa: implications for petrogenesis of carbonatites, Contrib. Mineral. Petrol. 146 (2004) 606–619.
[3] J.C. Alt, D.A.H. Teagle, The uptake of carbon during alteration of ocean crust, Geochim. Cosmochim. Acta 63 (1999) 1527–1535.
[4] R.D. Jarrard, Subduction fluxes of water, carbon dioxide, chlorine, and potassium, Geochem. Geophys. Geosyst. 4 (2003) 8905.
[5] G.M. Yaxley, D.H. Green, Experimental demonstration of refractory carbonate-bearing eclogite and siliceous melt in the subduction regime, Earth Planet. Sci. Lett. 128 (1994) 313–325.
[6] J.F. Molina, S. Poli, Carbonate stability and fluid composition in subducted oceanic crust: an experimental study on H_2O–CO_2-bearing basalts, Earth Planet. Sci. Lett. 176 (2000) 295–310.

[7] D.M. Kerrick, J.A.D. Connolly, Metamorphic devolatilization of subducted oceanic metabasalts: implications for seismicity, arc magmatism and volatile recycling, Earth Planet. Sci. Lett. 189 (2001) 19–29.
[8] M. Pertermann, M.M. Hirschmann, Partial melting experiments on a MORB-like pyroxenite between 2 and 3 GPa: constraints on the presence of pyroxenite in basalt source regions from solidus location and melting rate, J. Geophys. Res. 108 (2003) 2125.
[9] C.E. Manning, The chemistry of subduction-zone fluids, Earth Planet. Sci. Lett. 223 (2004) 1–16.
[10] J. Staudigel, T. Plank, B. White, H.U. Schmincke, Geochemical fluxes during seafloor alteration of the basaltic upper oceanic crust; DSDP sites 417 and 418, in: G.E. Bebout, D.W. Scholl, S.H. Kirby, J.P. Platt (Eds.), Subduction, Top to Bottom, Geophysical Monograph, vol. 96, American Geophysical Union, Washington, DC, 1996, pp. 19–38.
[11] J.C. Alt, Subseafloor processes in mid-ocean ridge hydrothermal systems, in: S.E. Humphris, R.E. Zierenberg, L.S. Mullineaux, R.E. Thomson (Eds.), Seafloor Hydrothermal Systems: Physical, Chemical, Biological, and Geological Interactions, Geophysical Monograph, vol. 95, American Geophysical Union, Washington, DC, 1995, pp. 85–114.
[12] G.J. Piermarini, S. Block, Ultrahigh pressure diamond-anvil cell and several semiconductor phase transition pressures in relation to fixed point pressure scale, Rev. Sci. Instrum. 46 (1975) 973–979.
[13] K. Bose, J. Ganguly, Quartz–coesite transition revisited—reversed experimental determination at 500–1200 °C and retrieved thermochemical properties, Am. Mineral. 80 (1995) 231–238.
[14] T. Yagi, M. Akaogi, O. Shimomura, T. Suzuki, S.-I. Akimoto, In situ observation of the olivine–spinel phase transformation in Fe_2SiO_4 using synchrotron radiation, J. Geophys. Res. 92 (1987) 6207–6213.
[15] J. Susaki, M. Akaogi, S. Akimoto, O. Shimomura, Garnet–perovskite transformation in $CaGeO_3$: in situ X-ray measurements using synchrotron radiation, Geophys. Res. Lett. 12 (1985) 729–732.
[16] J. Zhang, R.C. Liebermann, T. Gasparik, C.T. Herzberg, Melting and subsolidus relations of SiO_2 at 9–14 GPa, J. Geophys. Res. 98 (1993) 19785–19793.
[17] J.A. Dalton, B.J. Wood, The compositions of primary carbonate melt and their evolution through wallrock reaction in the mantle, Earth Planet. Sci. Lett. 119 (1993) 511–525.
[18] R.W. Luth, Diamonds, eclogites, and oxidation state of the Earth's mantle, Science 261 (1993) 66–68.
[19] G.M. Yaxley, D.H. Green, Experimental reconstruction of sodic dolomitic carbonatite melts from metasomatised lithosphere, Contrib. Mineral. Petrol. 124 (1996) 359–369.
[20] A.J. Irving, P.J. Wyllie, Subsolidus and melting relationships for calcite, magnesite and the join $CaCO_3$–$MgCO_3$ to 36 kb, Geochim. Cosmochim. Acta 39 (1975) 35–53.
[21] M. Pertermann, M.M. Hirschmann, Anhydrous partial melting experiments on MORB-like eclogite: phase relations, phase compositions and mineral–melt partitioning of major elements at 2–3 GPa, J. Petrol. 44 (2003) 2173–2201.
[22] M.M. Hirschmann, The mantle solidus: experimental constraints and the effect of peridotite composition, Geochem. Geophys. Geosyst. 1 (2000) DOI:10.1029/2000GC000070.
[23] N. Dellas, R. Dasgupta, M.M. Hirschmann, The effect of carbonate composition and concentration on the solidus of carbonated eclogite: an experimental study at 3 GPa, EOS Trans.-AGU 84 (2003) F1495 (abstract).
[24] H. Keppler, Water solubility in carbonatite melts, Am. Mineral. 88 (2003) 1822–1824.
[25] S.M. Peacock, Thermal structure and metamorphic evolution of subducting slabs, in: J. Eiler (Ed.), Inside the Subduction Factory, Geophysical Monograph, vol. 138, American Geophysical Union, Washington, DC, 2003, pp. 7–22.
[26] P.E. van Keken, B. Kiefer, S.M. Peacock, High-resolution models of subduction zones: implications for mineral dehydration reactions and the transport of water into the deep mantle, Geochem. Geophys. Geosyst. 3 (2003) DOI:10.1029/2002GC000256.
[27] M.W. Schmidt, S. Poli, Experimentally based water budgets for dehydrating slabs and consequences for arc magma generation, Earth Planet. Sci. Lett. 163 (1998) 361–379.
[28] J.F. Forneris, J.R. Holloway, Phase equilibria in subducting basaltic crust: implications for H_2O release from the slab, Earth Planet. Sci. Lett. 214 (2003) 187–201.
[29] I. Katayama, S. Nakashima, Hydroxyl in clinopyroxene from the deep subducted crust; evidence for H_2O transport into the mantle, Am. Min. 88 (2003) 229–234.
[30] J. Ita, L. Stixrude, Petrology, elasticity, and composition of the mantle transition zone, J. Geophys. Res. 97 (1992) 6849–6866.
[31] D.S. Chapman, Thermal gradients in the continental crust, in: J.B. Dawson, D.A. Carswell, J. Hall, K.H. Wedepohl (Eds.), The Nature of the Lower Continental Crust, Blackwell, London, 1986, pp. 63–70.
[32] A. Yasuda, T. Fujii, K. Kurita, Melting phase relations of anhydrous mid-ocean ridge basalt from 3 to 20 GPa: implications for the behavior of subducted oceanic crust in the mantle, J. Geophys. Res. 99 (1994) 9401–9414.
[33] D. Canil, C.M. Scarfe, Phase relations in peridotite + CO_2 systems to 12 GPa: implications for the origin of kimberlite and carbonate stability in the Earth's upper mantle, J. Geophys. Res. 95 (1990) 15805–15816.
[34] J.A. Dalton, D.C. Presnall, Carbonatitic melts along the solidus of model lherzolite in the system CaO–MgO–Al_2O_3–SiO_2–CO_2 from 3 to 7 GPa, Contrib. Mineral. Petrol. 131 (1998) 123–135.
[35] B.J. Wood, A. Pawley, D.R. Frost, Water and carbon in the earth's mantle, Philos. Trans. R. Soc. Lond. 354 (1996) 1495–1511.
[36] J. Revenaugh, S. Sipkin, Seismic evidence for silicate melt atop the 410-km mantle discontinuity, Nature 369 (1994) 474–476.
[37] L. Vinnik, V. Farra, Subcratonic low-velocity layer and flood basalts, Geophys. Res. Lett. 29 (2002) DOI:10.1029/2001GL014064.
[38] T.A. Song, D.B. Helmberger, S.P. Grand, Low-velocity zone atop the 410-km seismic discontinuity in the northwestern United States, Nature 427 (2004) 530–533.
[39] W.G. Minarik, E.B. Watson, Interconnectivity of carbonate melt at low melt fraction, Earth Planet. Sci. Lett. 133 (1995) 423–437.

[40] E.H. Hauri, N. Shimizu, J.J. Dieu, S.R. Hart, Evidence for hotspot-related carbonatite metasomatism in the oceanic upper mantle, Nature 365 (1993) 221–227.
[41] R.L. Rudnick, W.F. McDonough, B.W. Chappell, Carbonatite metasomatism in the northern Tanzanian mantle: petrographic and geochemical characteristics, Earth Planet. Sci. Lett. 114 (1993) 463–475.
[42] W.M. White, A.W. Hofmann, Sr and Nd isotope geochemistry of oceanic basalts and mantle evolution, Nature 296 (1982) 821–825.
[43] A.W. Hofmann, Chemical differentiation of the Earth: the relationship between mantle, continental crust, and oceanic crust, Earth Planet. Sci. Lett. 90 (1988) 297–314.
[44] T. Kogiso, Y. Tatsumi, G. Shimoda, G. Barsczus, High μ (HIMU) ocean island basalts in southern Polynesia: new evidence for whole mantle scale recycling of subducted oceanic crust, J. Geophys. Res. 102 (1997) 8085–8103.
[45] D. McKenzie, A. Stracke, J. Blichert-Toft, F. Albarède, K. Grönvold, R.K. O'Nions, Source enrichment processes responsible for isotopic anomalies in ocean island basalts, Geochim. Cosmochim. Acta 68 (2004) 2699–2724.
[46] K. Hoernle, G. Tilton, M.J. Le Bas, S. Duggen, D.G. Schönberg, Geochemistry of oceanic carbonatites compared with continental carbonatites: mantle recycling of oceanic crustal carbonate, Contrib. Mineral. Petrol. 142 (2002) 520–542.
[47] D.J. Schulze, B. Harte, J.W. Valley, J.M. Brenan, D.M.De.R. Channer, Extreme crustal oxygen isotope signatures preserved in coesite in diamond, Nature 423 (2003) 68–70.
[48] A.H. Treiman, E.J. Essene, Mantle eclogite and carbonate as sources of sodic carbonatites and alkalic magmas, Nature 302 (1983) 700–703.
[49] G.M. Yaxley, D.H. Green, V. Kamenetsky, Carbonatite metasomatism in the southern Australian lithosphere, J. Petrol. 39 (1998) 1917–1930.